PHOTONICS Research

Dielectric metalens-based Hartmann–Shack array for a high-efficiency optical multiparameter detection system

Yuxi Wang,[1,†] Zhaokun Wang,[1,†] Xing Feng,[1] Ming Zhao,[1] Cheng Zeng,[1] Guangqiang He,[2] Zhenyu Yang,[1,4] Yu Zheng,[3,5] and Jinsong Xia[1,6] [ID]

[1]Wuhan National Laboratory for Optoelectronics, School of Optical and Electronic Information, Huazhong University of Science and Technology (HUST), Wuhan 430074, China
[2]State Key Laboratory of Advanced Optical Communication Systems and Networks, Department of Electronic Engineering, Shanghai Jiao Tong University, Shanghai 200240, China
[3]State Key Laboratory of High Performance Complex Manufacturing, Central South University, Changsha 410083, China
[4]e-mail: zyang@hust.edu.cn
[5]e-mail: zhengyu@csu.edu.cn
[6]e-mail: jsxia@hust.edu.cn

The real-time measurement of the polarization and phase information of light is very important and desirable in optics. Metasurfaces can be used to achieve flexible wavefront control and can therefore be used to replace traditional optical elements to produce a highly integrated and extremely compact optical system. Here, we propose an efficient and compact optical multiparameter detection system based on a Hartmann–Shack array with 2×2 subarray metalenses. This system not only enables the efficient and accurate measurement of the spatial polarization profiles of optical beams via the inspection of foci amplitudes, but also measures the phase and phase-gradient profiles by analyzing foci displacements. In this work, details of the design of the elliptical silicon pillars for the metalens are described, and we achieve a high average focusing efficiency of 48% and a high spatial resolution. The performance of the system is validated by the experimental measurement of 22 scalar polarized beams, an azimuthally polarized beam, a radially polarized beam, and a vortex beam. The experimental results are in good agreement with theoretical predictions. © 2020 Chinese Laser Press

https://doi.org/10.1364/PRJ.383772

1. INTRODUCTION

The amplitude, phase, and state of polarization (SOP) are fundamental parameters for describing light waves. At present, however, most photodetectors are only sensitive to the light intensity, which makes traditional polarization and phase detection systems complex, bulky, and difficult to integrate. Metasurfaces are ultrathin two-dimensional metamaterials with subwavelength features that can flexibly manipulate the amplitude, phase, and SOP of the light. Over the last few years, metasurfaces have become a versatile platform for wavefront control. Metasurfaces have subwavelength thicknesses, which has been exploited to develop compact optical devices with metasurfaces, such as polarization elements [1–8], holograms [9–11], and metalenses [12–19]. Compared with traditional lenses, metalenses offer the advantages of higher compactness and no spherical aberrations. Therefore, research on metalenses is becoming one of the most popular directions in the field of metasurface-based optics. Numerous studies have been conducted on plasmonic metasurfaces [20–23]. These studies are fundamentally limited in terms of the efficiency of utilizing visible and NIR wavelengths for transmission operation, which poses a key obstacle to the practical application of metasurfaces. These problems can be solved by using dielectric metasurfaces [24–29]. Therefore, many novel metalenses based on dielectric metasurfaces have been reported recently, including dielectric polarization-dependent metalenses [30–34], dielectric polarization-independent metalenses [35–37], and broadband achromatic dielectric metalenses [38–40]. The fabrication of these planar lenses is straightforward, and the lenses can be vertically integrated and can potentially replace or complement their conventional refractive and diffractive counterparts, facilitating further miniaturization of high-performance optical devices and systems.

In a previous work, we demonstrated a dielectric metalens array for multiparameter detection operating at 1550 nm [41]. The unit elements of the metalenses are composed of elliptical

silicon pillars. Each pixel of the array consists of six different metalenses that can converge differently polarized light onto the focal plane. The phase gradient and the SOP of the incident beam can be measured by detecting the positions and intensities of the focal points.

Here, we continue this research and propose and experimentally verify a new type of metalens array operating at 1550 nm. Each pixel of the silicon-based metalens array consists of a 2×2 submetalens array that replaces the previous 3×2 submetalens array. This configuration affords a 1.5-fold theoretical improvement in the spatial resolution, which is beneficial for applications in optical imaging and optical detection. In addition, by redesigning the unit cell of each metalens (i.e., by reducing the lattice constant from 1.5 to 1.0 µm and optimizing the unit element size for higher transmittance), we significantly improve the average focusing efficiency from 28% to 48%. In the experiments, we first accurately characterize the SOP of 22 different incident-polarized beams by one pixel of the array. The average relative error between the theoretical results and experimental results is as small as 4.24%. Next, we detect two common light beams with nonconstant SOPs (a radially polarized beam and an azimuthally polarized beam) and a vortex light beam with a spiral wavefront, demonstrating that our design is also applicable to beams with complex SOPs and wavefronts. The experimental results are in good agreement with the theoretical values.

2. PRINCIPLE AND DESIGN

The proposed optical multiparameter detection system is shown in Fig. 1 and consists of two components. The first

and most important component is a dielectric metalens array. The second component is a camera (Xenics, Bobcat-320-GigE) that is placed on the focal plane of the metalens array. The incident beam is focused by the dielectric metalens array. Then, the phase and SOP profiles of the beam can be derived from the position and intensity information of each focal spot that is detected by the camera.

The metalens array contains multiple pixels, and each pixel can function independently to reconstruct the phase gradient and SOP of the corresponding area of the incident beam. Figure 2 shows the principle and structure of the metalens array. Each pixel contains four different metalenses that can separate four differently polarized components from the incident beam and converge these components onto the camera. In Fig. 2(a), I_x, I_y, I_a, and I_l denote the intensities of the horizontal, vertical, 45 deg, and left-circularly polarized components, respectively. The intensities of the differently polarized components are detected by the camera, after which the Stokes parameters of the incident beams are reconstructed. At the same time, the phase profile of the incident beams is obtained by detecting the position of the focal spots (d_x and d_y refer to the position shifts between the projection of the center of the metalens and the corresponding focal points along the x and y axes, respectively).

As shown in Fig. 2(b), the unit element of the metalens is an elliptical silicon pillar that is placed on a layer of silica with a constant height $H = 340$ nm and a square lattice constant $a = 1000$ nm. The primary function of the pillar is to locally
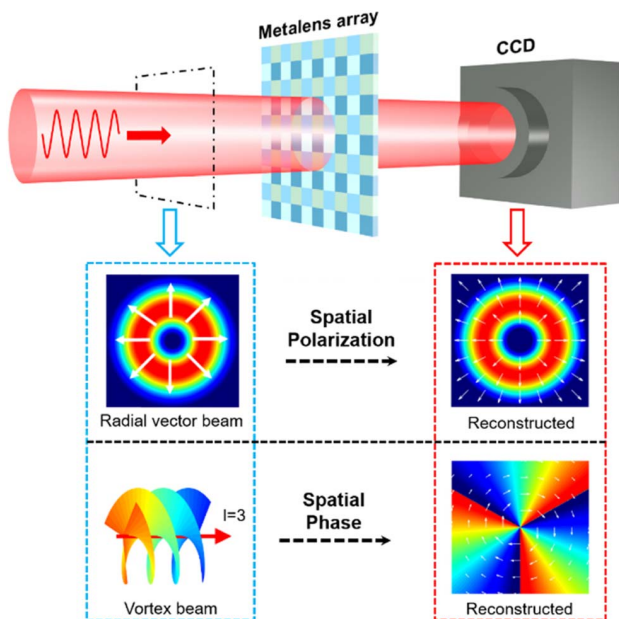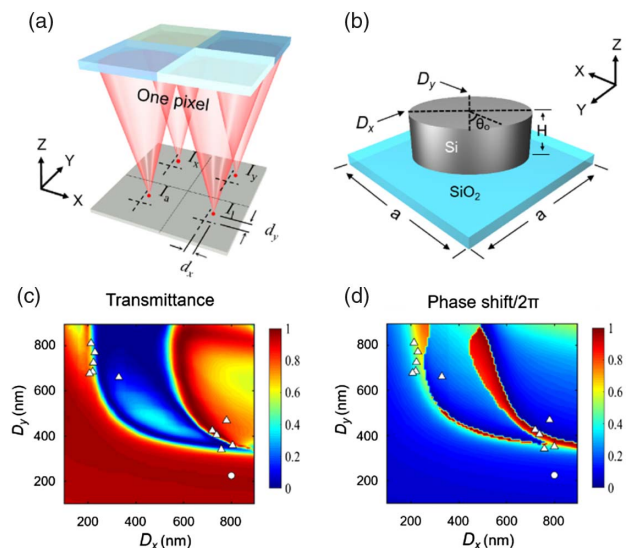

Fig. 1. Schematic shows the dielectric metalens-based Hartmann–Shack array for a high-efficiency optical multiparameter detection system. The system can simultaneously measure the spatial polarization and phase profiles of optical beams. The colors are only used to enhance the clarity of the image and to distinguish metalenses with different polarization sensitivities in the array.

Fig. 2. Schematic and design of metalenses. (a) Scheme for one pixel of a metalens array. (The colors indicate different polarizations.) The dotted crosses on the focal plane correspond to the centers of particular metalenses. (b) Scheme for one unit element of a metalens; (c), (d) simulation results for intensity transmittance and phase shifts of unit elements under normal incidence of y-polarized light. The white triangles indicate the transmittance, phase, and dimensions of 11 elliptical silicon pillars along the x-positive axis from the center of a y-polarized metalens. The white circle at ($D_x = 800$ nm, $D_y = 224$ nm) highlights the structural parameters used for an l-polarized sensitive metalens.

shift the phase of the incident light. The wavefront of the transmitted beam can be flexibly manipulated by adjusting the spatial scales of the geometrical parameters (the major axis D_x, the minor axis D_y, and the orientation angle θ_o). The finite-difference time-domain (FDTD) method (Lumerical Inc. FDTD Solutions) is applied to calculate and analyze the characteristics of the unit element to manipulate the amplitude and phase of the incident beam. Figures 2(c) and 2(d) show the intensity transmittance and the phase shifts of the unit element for different dimensions when the y-polarized light is incident normally. These data are combined with the following methods to obtain a blueprint for one pixel of the metalens array. To design a flat focusing lens for a prescribed light polarization, the phase shift of the respective polarized component that is introduced by each elliptical silicon pillar in the x–y plane must satisfy Eq. (1) [14],

$$\varphi(x,y) = -\frac{2\pi}{\lambda} \cdot \left(\sqrt{x^2 + y^2 + f^2} - f \right) + \text{const}, \quad \textbf{(1)}$$

where f denotes the focal length of the lens, λ denotes the working wavelength, and $\varphi(x,y)$ denotes the phase that is needed at the (x,y) location of each elliptical silicon pillar in the x–y plane. The constant denotes the phase of the elliptical silicon pillar at the center, which is just a reference phase and is set to 0 here. In this study, the focal length and the working wavelength are positioned at 30 μm and 1550 nm, respectively.

The design of the metalens array consists of two components—a linearly polarized sensitive metalens and a circularly polarized sensitive metalens, which are based on propagation phase theory and Pancharatnam–Barry (PB) phase theory [42–44]. The dimensions of all the selected elliptical silicon pillars for the metalenses are based on the following three conditions. (1) The dimensions (D_x and D_y) of all the selected elliptical silicon pillars should be polarization-dependent. (2) The local phase of all the selected elliptical silicon pillars should satisfy phase Eq. (1). (3) Once conditions (1) and (2) are satisfied, elliptical silicon pillars with high transmittance are selected as much as possible. The design of a linearly polarized sensitive metalens depends mainly on propagation phase theory. Phase coverage over the 0–2π range can be achieved by changing the dimensions of the unit element. Taking the y-polarized sensitive metalens as a theoretical design example, the structural data points with the higher intensity transmittance in Fig. 2(c) are selected as much as possible, while ensuring that each selected elliptical silicon pillar satisfies the above-mentioned conditions (1) and (2). To provide more details on the design of the elliptical silicon pillars, the 11 elliptical silicon pillars along the x-positive axis from the center of the metalens are demarcated in Figs. 2(c) and 2(d). Although the transmittance of several elliptical silicon pillars is not high, this is the highest transmittance that can be obtained while meeting the polarization dependence and local phase requirements. Our goal is to choose as many elliptical silicon pillars with as high transmittance as possible that can satisfy the first two conditions. Then, x-polarized and a-polarized metalenses are realized by performing 90 deg and −45 deg rotations of these silicon pillars, respectively.

In addition, the PB phase shift is adopted to design a metalens for circularly polarized light. All the unit elements have the same dimensions with $D_x = 800$ nm and $D_y = 224$ nm, which is demarcated by the white circle in Figs. 2(c) and 2(d), and phase variation is achieved via the rotation of these unit elements. Equation (2) is derived from the Jones matrix calculus, and it describes the complex amplitudes of the transmitted light for l-polarized incident light [15],

$$t_l = \frac{t_o + t_e}{2} \cdot \begin{pmatrix} 1 \\ i \end{pmatrix} + \frac{t_o - t_e}{2} \cdot \exp(i \cdot 2\theta_o) \cdot \begin{pmatrix} 1 \\ -i \end{pmatrix}. \quad \textbf{(2)}$$

Here, t_o and t_e denote the complex transmission coefficients of the linearly polarized incident beam along the major and minor axes of the elliptical silicon pillars, and θ_o denotes the orientation angle in the counterclockwise direction. The additional phase shift increases linearly from 0 to 2π as θ_o varies from 0 to π. The transmittance is improved by making the first group of terms (which have the same handedness as the incident light) vanish by choosing the smallest absolute value of $t_o + t_e$ and maximizing the second group of terms (which have the opposite handedness to the incident light) by choosing the largest absolute value of $t_o - t_e$ [see the white circle at (800 nm, 224 nm) in Figs. 2(c) and 2(d)]. Compared with the previous consideration of only making the first terms vanish, the total transmittance has been improved. Under this condition, the incident light is almost completely converted into the opposite circular-handedness that can be manipulated by the PB phase shift, which improves the efficiency of the circular polarization conversion. More importantly, this procedure increases the transmittance of each elliptical silicon pillar and maximizes the efficiency of the corresponding circularly polarized incident light. The additional phase shift spans the 0–2π range by varying the rotation angle of the elliptical silicon pillars, and the transmittance of each elliptical silicon pillar is greater than 0.7. All the unit elements of the metalens for the l-polarized components are obtained in this manner.

The dielectric metalens array is fabricated using complementary metal-oxide-semiconductor (CMOS)-compatible nanofabrication techniques. Figure 3 shows scanning electron micrographs and optical intensity distributions for the fabricated metalens array. Scanning electron micrographs with different magnifications are shown in Figs. 3(a)–3(d). Each pixel consists of four different metalenses that are designed for four differently polarized components (x, y, a, and l). All the metalenses have a footprint of 21 μm × 21 μm and the same focal length of 30 μm, which results in a numerical aperture (NA) of 0.33. Figures 3(e) and 3(f) show the optical intensity distributions for the y- and l-polarized metalenses, respectively.

The focusing efficiency is defined as the ratio of the light power of the focal spot to the power collected by the camera on a metalens; this value is 41% for a linearly polarized metalens and 55% for a circularly polarized metalens, and different from the theoretical predictions of 69% and 72%. The deviation between the experimental results and theoretical predictions can be attributed to fabrication errors and imperfections in the optical components. To eliminate the deviation, on the one hand, it is possible to optimize the structure with
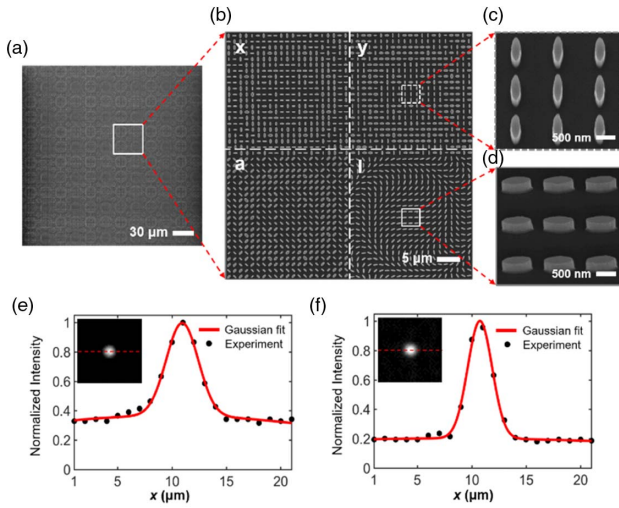
Fig. 3. Scanning electron micrographs and intensity distributions of a manufactured metalens array. (a) Local scanning electron micrograph of a fabricated metalens array. The white rectangle indicates one pixel of the array. (b) Corresponding magnified scanning electron micrograph of one pixel, where the polarization bases are denoted by letters for each metalens; (c)–(d) oblique view of the selected parts of the metalenses; (e)–(f) intensity profiles along the x axis, passing through the focus, together with a Gaussian fit for the y-polarized sensitive metalens and l-polarized sensitive metalens; the diameter of the focal spot is 7 µm.

high dimensional tolerance; on the other hand, the structural dimensions can be calibrated and corrected by scanning electron microscopy during the manufacturing process to ensure that they are as close to the theoretical values as possible. The improvement in the focusing efficiency can be explained by the following two considerations. The first consideration is that the reduction in the lattice constant from 1.5 µm to 1.0 µm increases the density of the elliptical silicon pillars in a metalens of the same size. Increasing the number of elliptical silicon pillars smooths out the phase gradient across the metalens: more elliptical silicon pillars participate in the manipulation of the incident beam to form the phase required for focusing, which helps to improve the focusing efficiency. Note, however, that although the focusing efficiency of the metalens can be improved by decreasing the lattice constant to increase the number of elliptical silicon pillars, the lattice constant cannot be reduced infinitely. A reduction in the lattice constant inevitably leads to a reduction in the dimensions of the elliptical silicon pillars, which increases the difficulty of the manufacturing process to a certain extent. Therefore, taking both of the above-mentioned considerations into account, we select a lattice constant of 1.0 µm instead of the original value of 1.5 µm. Second, we select dimensions for the unit elliptical silicon pillar so that the pillar has a higher transmittance to satisfy the local phase requirement and polarization dependence. The increased transmittance of the unit elliptical silicon pillar means that more incident light has been utilized, which also helps to improve the focusing efficiency.

Generally, the SOP can be determined from the Stokes parameters, which can be obtained by using Eq. (3) [45,46],

$$
\begin{aligned}
S_0 &= I_x + I_y, \\
S_1 &= I_x - I_y, \\
S_2 &= I_a - I_b, \\
S_3 &= I_r - I_l,
\end{aligned}
\tag{3}
$$

where (S_0, S_1, S_2, S_3) are the four components of the Stokes parameters. The intensities of the six polarization components $(I_x, I_y, I_a, I_b, I_l, I_r)$ refer to the intensities of the horizontal, vertical, +45 deg, –45 deg, left-circular, and right-circular polarization components of the incident beam, respectively. Note that the Stokes parameters that are described above are calculated based on the intensities of six polarization components, whereas only three types of linear polarization components and one circular polarization component are needed to reconstruct the Stokes parameters [33]. And then the Stokes parameters can be rewritten as Eq. (4). Moreover, the spatial resolution can be effectively improved by 1.5-fold with this method,

$$
\begin{aligned}
S_0 &= I_x + I_y, \\
S_1 &= I_x - I_y, \\
S_2 &= 2I_a - I_x - I_y, \\
S_3 &= 2I_l - I_x - I_y.
\end{aligned}
\tag{4}
$$

For locally linearly polarized light, the Stokes parameters can be characterized by the polarization angle θ_p,

$$
\theta_p = \frac{1}{2} \arctan \frac{S_2}{S_1}.
\tag{5}
$$

In addition, this detection system is similar to a Hartmann–Shack wavefront sensor [47,48] and can detect the phase gradients of an incident beam, which can be calculated by using Eqs. (6) and (7),

$$
\frac{\partial \phi}{\partial x} = \frac{2\pi}{\lambda} \cdot \frac{d_x}{\sqrt{f^2 + d_x^2}},
\tag{6}
$$

$$
\frac{\partial \phi}{\partial y} = \frac{2\pi}{\lambda} \cdot \frac{d_y}{\sqrt{f^2 + d_y^2}}.
\tag{7}
$$

In the equations above, $\partial \phi / \partial x$ and $\partial \phi / \partial y$ denote the phase slopes of a wavefront in the x and y directions, and d_x and d_y denote the position shifts of the focus. The wavefront of the incident beam can be reconstructed by calculating and analyzing the focus shifts and phase gradients.

3. EXPERIMENTAL RESULTS

A. SOP Detection

The feasibility of the polarization reconstruction method is verified by experimentally detecting and reconstructing incident beams with 22 different SOPs. Figure 4(a) shows the optical setup for polarization detection. Figure 4(b) shows the intensity distributions of six differently polarized incident beams in one pixel. To ensure experimental accuracy, four incident x-, y-, a-, and l-polarized beams serve as reference states
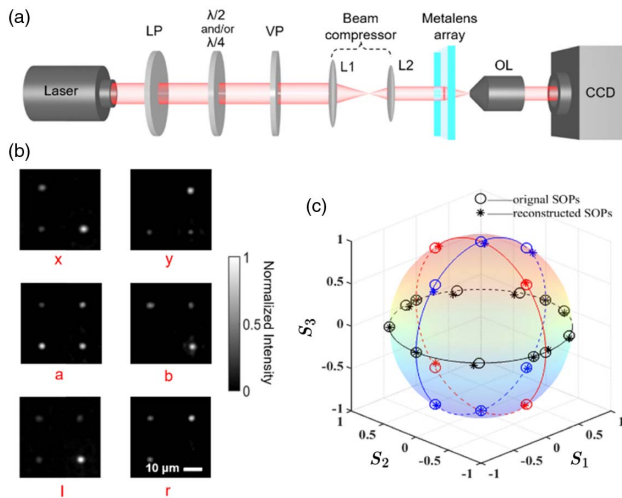
Fig. 4. Experimental validation of SOP detection with one pixel. (a) Optical setup for polarization detection. LP, linear polarization; $\lambda/4$, quarter-wave plate; $\lambda/2$, half-wave plate; VP, vector wave plate; L1, L2, lens; OL, 20× objective lens; CCD, charge-coupled device. (b) Intensity distributions of the focal points in one pixel for incident horizontal or vertical linear polarization ("x" and "y"), diagonal linear polarization ("a" and "b"), and circular polarization ("l" and "r"); (c) experimentally reconstructed (stars) Stokes parameters (S_1, S_2, S_3) and theoretical predictions (small circles) are compared on a Poincaré sphere (see Data File 1).

Fig. 5. Detection and reconstruction of two vector beams. (a), (b) Intensity distributions for two vector beams. The blue arrows denote the local SOPs. (c), (d) Raw data of measured focal points for two vector beams; (e), (f) reconstructed polarization profiles. The black arrows correspond to the measured local polarization vectors, and the red arrows correspond to the theoretical predictions. The dashed gray lines are drawn to identify individual pixels.

in the system calibration. Numerical calculations are performed based on these reference states, and a reconstructed matrix is obtained for reconstructing the Stokes parameters. As shown in Fig. 4(c), the SOPs of the 22 incident beams are completely reconstructed and compared with the theoretical results on a Poincaré sphere. The average relative error is 4.24%, which may be attributed to fabrication imperfections in the device. More reference states could be used to further improve the performance, but as more pixel elements are required for each polarization measurement, the spatial resolution would be impaired. Furthermore, each of the pixels of the polarization measurement samples the scene slightly differently, which increases the systematic error because of the difference in the gain of the pixels.

The applicability of the spatial SOP detection of the system is indicated by performing experiments on two common beams with nonconstant SOPs (a radially polarized beam and an azimuthally polarized beam). Figures 5(a) and 5(b) show the intensity distributions for the two vector beams that are recorded by the camera. The intensity distributions of the focal points of the 5 × 7 pixels metalens array are shown in Figs. 5(c) and 5(d). Apart from the pixels near the central singularities, the focal points of all the pixels can be clearly observed. We apply the raw data of the focal points to Eq. (5) to obtain $\theta_p(x, y)$ for the locally polarized light. The experimental results (black arrows) clearly agree very well with the theoretical results (red arrows), as shown in Figs. 5(e) and 5(f). The error is defined as the ratio of the angle between the two arrows and 90 deg, which indicates the coincidence degree of the two arrows. The average detection error of the radially polarized beam is 6.28%, and that of the azimuthally polarized beam is 2.49%. The slight
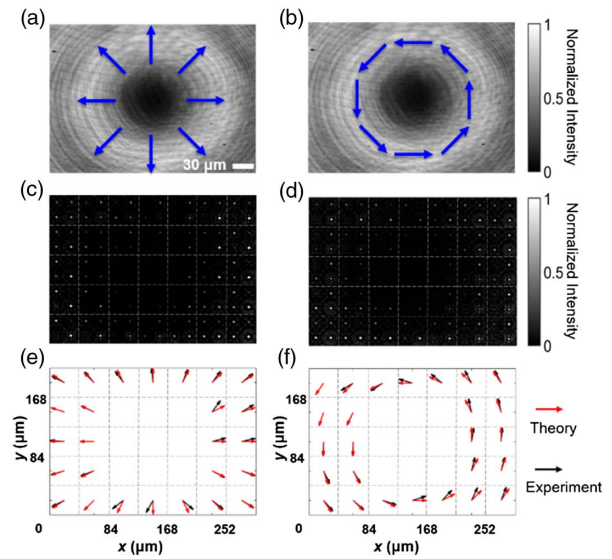
difference between the two average errors may be attributed to systematic measurement error. The experimental results show that the pixel with the largest error is found in the lower right part of Figs. 5(e) and 5(f), and this error is caused by small stray points that have been introduced by reflection between the optics.

B. Wavefront Measurement

It is well known that the usual Hartmann–Shack wavefront sensors cannot be used to detect and analyze the SOP of an incident beam. However, since our design principle for a metalens array is related to Hartmann–Shack theory, the system can naturally be applied to obtain phase profiles. The wavefront detection performance of the system is validated by using a vortex beam that is generated by a liquid crystal spatial light modulator and has a twisted wavefront and a topological charge of 20. Figure 6(a) shows the optical setup for vortex beam detection. The intensity distribution of the incident vortex beam that is recorded by the camera is shown in Fig. 6(b). Note that the metalens array for vortex beam profiling consists of 5 × 6 pixels. The raw data of the focal points positions are shown in Fig. 6(c). The intensities of the focal points are clearly weak in the center and corners of the image, causing the focal points to be circularly distributed. In addition, the intensity of the focus of the y-polarized sensitive metalens is much stronger than that of the other focal points, especially for the x-polarized metalens, which indicates that the SOP of the vortex beam is almost y-polarized. The results agree well with the theoretical predictions. The position shifts of the focal points are calculated by a standard centroid algorithm and then the phase gradient distribution of the incident beam that is calculated by using Eqs. (6) and (7). Based on the
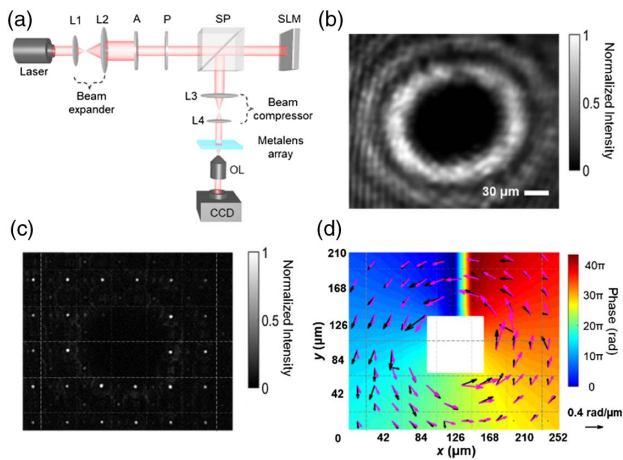
Fig. 6. Detection and reconstruction of the vortex beam. (a) Schematic of the optical setup. L1, L2, L3, L4, lens; A, aperture; P, polarizer; SP, splitter prism; SLM, spatial light modulator; and OL, objective lens. (b) Intensity distribution for the vortex beam; (c) raw data of measured focal points for the vortex beam; (d) phase gradients (pink arrows denote theoretical results, and black arrows denote experimental results) and reconstructed wavefront (false-color scale) of the vortex beam. The dashed lines are drawn in above images to distinguish individual pixels of the metalens array. The length of the reference arrow is 0.4 rad/μm.

method of zonal estimation and Southwell geometry [49], these gradients are used to reconstruct the wavefront of the vortex beam by integrating, which is shown in Fig. 6(d). The white squares correspond to pixels near the center of the vortex beam where the beam intensity is near zero. The calculated topological charge of the vortex beam is 18.72, which corresponds to a relative error of 6.4% compared to the theoretical value of 20. This result validates the system for the detection of beams with complex wavefronts. In this experiment, the metalens focus generally has a small displacement. Therefore, natural jitter can affect the experimental results. Moreover, the SOP of the incident beam can be determined from the intensities of the focal points that are obtained from the wavefront measurement. In essence, SOP detection and wavefront measurement are based on different principles, which can be operated both independently of each other and simultaneously.

4. CONCLUSION

Note that although the above-mentioned experiments for polarization reconstruction and phase detection are carried out separately, the system can realize the measurements of polarization states and wavefront profiles simultaneously, which was confirmed in our last study and is also discussed in the wavefront measurement section of this study. Moreover, because the degree of polarization can be obtained by using the measured Stokes parameters, the system is also clearly suitable for partially polarized beams.

The 2 × 2 metalens array proposed in this study has a higher spatial resolution and focusing efficiency than the previously developed 3 × 2 structure. Compression of the 3 × 2 subarray into a 2 × 2 subarray results in a 50% increase in the spatial resolution. For linearly incident polarizations, we measured

an average focusing efficiency of 41%, which is higher than the previous measurement of 30%. For circularly incident polarization, the focusing efficiency is increased to 55%, which is superior to the previous value of 26%. The increase in efficiency can be attributed to the following two considerations. The first consideration is that reducing the lattice constant from 1.5 μm to 1.0 μm increases the density of the silicon nanopillars in a metalens of the same size and smooths out the phase gradient across the metalens. A larger number of elliptical silicon pillars participate in the manipulation of the incident beam to form the phase required for focusing, which helps to improve the focusing efficiency. The second consideration is that the dimensions of the selected unit elliptical silicon pillar increase the transmittance by satisfying the focus phase requirement and polarization dependence. The increased transmittance of the unit elliptical silicon pillar means that more incident light is utilized, which also helps to improve the focusing efficiency. For a linearly polarized metalens, elliptical silicon pillars with high transmittance are selected as much as possible. For an l-polarized metalens, we maximize the second group of terms in Eq. (2) by choosing the largest absolute value of $t_o - t_e$, while selecting the smallest possible value for $t_o + t_e$ in the first group of terms. Under this condition, the incident light is almost completely converted into the opposite circular-handedness, and the transmittance of the unit elliptical silicon pillar is increased. It is well known that focusing efficiency and resolution are critical in optical imaging and optical probing. The increase in the focusing efficiency shows that more incident light is utilized, enabling weaker signals to be detected. The improvement in the resolution can further enrich the details of the incident light and increase the detection capability of the device. The improvement in the focusing efficiency and resolution helps to increase the accuracy of the measurement of the incident light and to increase the detection capability of the device. In the experiments, the average measurement error of the scalar polarized beams is 4.24%, which is smaller than our previously obtained value of 4.83%. For two vector-polarized beams (a radially polarized beam and an azimuthally polarized beam), the measurement errors are 6.28% and 2.49%, respectively, which are better than our previously obtained values of 6.33% and 4.46%. The measurement error in the vortex beam detection is 6.4%, and our previously obtained value was 8.0%.

In summary, in this study, we have demonstrated the operation of an optical multiparameter detection system based on an all-dielectric metalens array at 1550 nm. Each pixel of the metalens array consists of four differently polarized sensitive metalenses. By measuring the intensities and positions of the focal points, the system can realize the real-time detection of the SOP and wavefront distributions of the incident light.

Characterization (CMFC) in the Wuhan National Laboratory for Optoelectronics (WNLO) of Huazhong University of Science and Technology (HUST).

†These authors contributed equally to this work.

REFERENCES

1. J. Lin, J. P. B. Mueller, Q. Wang, G. Yuan, N. Antoniou, X.-C. Yuan, and F. Capasso, "Polarization-controlled tunable directional coupling of surface plasmon polaritons," Science **340**, 331–334 (2013).
2. A. Pors, M. G. Nielsen, and S. I. Bozhevolnyi, "Plasmonic metagratings for simultaneous determination of Stokes parameters," Optica **2**, 716–723 (2015).
3. M. Pu, X. Li, X. Ma, Y. Wang, Z. Zhao, C. Wang, C. Hu, P. Gao, C. Huang, H. Ren, X. Li, F. Qin, J. Yang, M. Gu, M. Hong, and X. Luo, "Catenary optics for achromatic generation of perfect optical angular momentum," Sci. Adv. **1**, e1500396 (2015).
4. Z. Zhao, M. Pu, H. Gao, J. Jin, X. Li, X. Ma, Y. Wang, P. Gao, and X. Luo, "Multispectral optical metasurfaces enabled by achromatic phase transition," Sci. Rep. **5**, 15781 (2015).
5. J. P. Balthasar Mueller, K. Leosson, and F. Capasso, "Ultracompact metasurface in-line polarimeter," Optica **3**, 42–47 (2016).
6. W. T. Chen, P. Torok, M. R. Foreman, C. Y. Liao, W. Y. Tsai, P. R. Wu, and D. P. Tsai, "Integrated plasmonic metasurfaces for spectropolarimetry," Nanotechnology **27**, 224002 (2016).
7. P. C. Wu, W.-Y. Tsai, W. T. Chen, Y.-W. Huang, T.-Y. Chen, J.-W. Chen, C. Y. Liao, C. H. Chu, G. Sun, and D. P. Tsai, "Versatile polarization generation with an aluminum plasmonic metasurface," Nano Lett. **17**, 445–452 (2017).
8. S. Luo, Q. Li, Y. Yang, X. Chen, W. Wang, Y. Qu, and M. Qiu, "Controlling fluorescence emission with split-ring-resonator-based plasmonic metasurfaces," Laser Photon. Rev. **11**, 1600299 (2017).
9. G. X. Zheng, H. Muhlenbernd, M. Kenney, G. X. Li, T. Zentgraf, and S. Zhang, "Metasurface holograms reaching 80% efficiency," Nat. Nanotechnol. **10**, 308–312 (2015).
10. W. Ye, F. Zeuner, X. Li, B. Reineke, S. He, C.-W. Qiu, J. Liu, Y. Wang, S. Zhang, and T. Zentgraf, "Spin and wavelength multiplexed nonlinear metasurface holography," Nat. Commun. **7**, 11930 (2016).
11. X. Li, L. Chen, Y. Li, X. Zhang, M. Pu, Z. Zhao, X. Ma, Y. Wang, M. Hong, and X. Luo, "Multicolor 3D meta-holography by broadband plasmonic modulation," Sci. Adv. **2**, e1601102 (2016).
12. H. F. Shi, C. T. Wang, C. L. Du, X. G. Luo, X. C. Dong, and H. T. Gao, "Beam manipulating by metallic nano-slits with variant widths," Opt. Express **13**, 6815–6820 (2005).
13. L. Verslegers, P. B. Catrysse, Z. Yu, J. S. White, E. S. Barnard, M. L. Brongersma, and S. Fan, "Planar lenses based on nanoscale slit arrays in a metallic film," Nano Lett. **9**, 235–238 (2009).
14. F. Aieta, P. Genevet, M. A. Kats, N. Yu, R. Blanchard, Z. Gahurro, and F. Capasso, "Aberration-free ultrathin flat lenses and axicons at telecom wavelengths based on plasmonic metasurfaces," Nano Lett. **12**, 4932–4936 (2012).
15. X. Chen, L. Huang, H. Muehlenbernd, G. Li, B. Bai, Q. Tan, G. Jin, C.-W. Qiu, S. Zhang, and T. Zentgraf, "Dual-polarity plasmonic metalens for visible light," Nat. Commun. **3**, e1601102 (2012).
16. A. Pors, M. G. Nielsen, R. L. Eriksen, and S. I. Bozhevolnyi, "Broadband focusing flat mirrors based on plasmonic gradient metasurfaces," Nano Lett. **13**, 829–834 (2013).
17. S. Zhang, M.-H. Kim, F. Aieta, A. She, T. Mansuripur, I. Gabay, M. Khorasaninejad, D. Rousso, X. Wang, M. Troccoli, N. Yu, and F. Capasso, "High efficiency near diffraction-limited mid-infrared flat lenses based on metasurface reflectarrays," Opt. Express **24**, 18024–18034 (2016).
18. J. Hu, C.-H. Liu, X. Ren, L. J. Lauhon, and T. W. Odom, "Plasmonic lattice lenses for multiwavelength achromatic focusing," ACS Nano **10**, 10275–10282 (2016).
19. S. Wang, P. C. Wu, V. C. Su, Y. C. Lai, C. Hung Chu, J. W. Chen, S. H. Lu, J. Chen, B. Xu, C. H. Kuan, T. Li, S. Zhu, and D. P. Tsai, "Broadband achromatic optical metasurface devices," Nat Commun. **8**, 187 (2017).
20. N. Yu, P. Genevet, M. A. Kats, F. Aieta, J.-P. Tetienne, F. Capasso, and Z. Gaburro, "Light propagation with phase discontinuities: generalized laws of reflection and refraction," Science **334**, 333–337 (2011).
21. F. Monticone, N. M. Estakhri, and A. Alu, "Full control of nanoscale optical transmission with a composite metascreen," Phys. Rev. Lett. **110**, 203903 (2013).
22. N. Yu and F. Capasso, "Flat optics with designer metasurfaces," Nat. Mater. **13**, 139–150 (2014).
23. N. Meinzer, W. L. Barnes, and I. R. Hooper, "Plasmonic meta-atoms and metasurfaces," Nat. Photonics **8**, 889–898 (2014).
24. S. Jahani and Z. Jacob, "All-dielectric metamaterials," Nat. Nanotechnol. **11**, 23–36 (2016).
25. A. I. Kuznetsov, A. E. Miroshnichenko, M. L. Brongersma, Y. S. Kivshar, and B. Luk'yanchuk, "Optically resonant dielectric nanostructures," Science **354**, aag2472 (2016).
26. M. Khorasaninejad and F. Capasso, "Metalenses: versatile multifunctional photonic components," Science **358**, eaam8100 (2017).
27. P. Genevet, F. Capasso, F. Aieta, M. Khorasaninejad, and R. Devlin, "Recent advances in planar optics: from plasmonic to dielectric metasurfaces," Optica **4**, 139–152 (2017).
28. P. Lalanne and P. Chavel, "Metalenses at visible wavelengths: past, present, perspectives," Laser Photon. Rev. **11**, 1600295 (2017).
29. P. Huo, S. Zhang, Q. Fan, Y. Lu, and T. Xu, "Photonic spin-controlled generation and transformation of 3D optical polarization topologies enabled by all-dielectric metasurfaces," Nanoscale **11**, 10646–10654 (2019).
30. D. Fattal, J. Li, Z. Peng, M. Fiorentino, and R. G. Beausoleil, "Flat dielectric grating reflectors with focusing abilities," Nat. Photonics **4**, 466–470 (2010).
31. D. Lin, P. Fan, E. Hasman, and M. L. Brongersma, "Dielectric gradient metasurface optical elements," Science **345**, 298–302 (2014).
32. M. Khorasaninejad, W. T. Chen, R. C. Devlin, J. Oh, A. Y. Zhu, and F. Capasso, "Metalenses at visible wavelengths: diffraction-limited focusing and subwavelength resolution imaging," Science **352**, 1190–1194 (2016).
33. S. Wei, Z. Yang, and M. Zhao, "Design of ultracompact polarimeters based on dielectric metasurfaces," Opt. Lett. **42**, 1580–1583 (2017).
34. E. Arbabi, S. M. Kamali, A. Arbabi, and A. Faraon, "Full-Stokes imaging polarimetry using dielectric metasurfaces," ACS Photon. **5**, 3132–3140 (2018).
35. S. Vo, D. Fattal, W. V. Sorin, Z. Peng, T. Tho, M. Fiorentino, and R. G. Beausoleil, "Sub-wavelength grating lenses with a twist," IEEE Photon. Technol. Lett. **26**, 1375–1378 (2014).
36. A. Arbabi, Y. Horie, A. J. Ball, M. Bagheri, and A. Faraon, "Subwavelength-thick lenses with high numerical apertures and large efficiency based on high-contrast transmitarrays," Nat. Commun. **6**, 7069 (2015).
37. M. Khorasaninejad, A. Y. Zhuit, C. Roques-Carmes, W. T. Chen, J. Oh, I. Mishra, R. C. Devlin, and F. Capasso, "Polarization-insensitive metalenses at visible wavelengths," Nano Lett. **16**, 7229–7234 (2016).
38. F. Aieta, M. A. Kats, P. Genevet, and F. Capasso, "Multiwavelength achromatic metasurfaces by dispersive phase compensation," Science **347**, 1342–1345 (2015).
39. W. T. Chen, A. Y. Zhu, V. Sanjeev, M. Khorasaninejad, Z. Shi, E. Lee, and F. Capasso, "A broadband achromatic metalens for focusing and imaging in the visible," Nat. Nanotechnol. **13**, 220–226 (2018).
40. S. Wang, P. C. Wu, V.-C. Su, Y.-C. Lai, M.-K. Chen, H. Y. Kuo, B. H. Chen, Y. H. Chen, T.-T. Huang, J.-H. Wang, R.-M. Lin, C.-H. Kuan, T. Li, Z. Wang, S. Zhu, and D. P. Tsai, "A broadband achromatic metalens in the visible," Nat. Nanotechnol. **13**, 227–232 (2018).
41. Z. Yang, Z. Wang, Y. Wang, X. Feng, M. Zhao, Z. Wan, L. Zhu, J. Liu, Y. Huang, J. Xia, and M. Wegener, "Generalized Hartmann–Shack array of dielectric metalens sub-arrays for polarimetric beam profiling," Nat. Commun. **9**, 4607 (2018).
42. M. V. Berry, "The adiabatic phase and Pancharatnam's phase for polarized light," J. Mod. Opt. **34**, 1401–1407 (1987).

43. E. Hasman, V. Kleiner, G. Biener, and A. Niv, "Polarization dependent focusing lens by use of quantized Pancharatnam–Berry phase diffractive optics," Appl. Phys. Lett. **82**, 328–330 (2003).

44. J. P. B. Mueller, N. A. Rubin, R. C. Devlin, B. Groever, and F. Capasso, "Metasurface polarization optics: independent phase control of arbitrary orthogonal states of polarization," Phys. Rev. Lett. **118**, 113901 (2017).

45. F. Gori, "Measuring Stokes parameters by means of a polarization grating," Opt. Lett. **24**, 584–586 (1999).

46. A. Pors and S. I. Bozhevolnyi, "Waveguide metacouplers for in-plane polarimetry," Phys. Rev. Appl. **5**, 064015 (2016).

47. B. C. Platt and R. Shack, "History and principles of Shack–Hartmann wavefront sensing," J. Refractive Surg. **17**, S573–S577 (2001).

48. R. Tyson, *Principles of Adaptive Optics*, 3rd ed. (CRC Press, 2010).

49. W. H. Southwell, "Wave-front estimation from wave-front slope measurements," J. Opt. Soc. Am. **70**, 998–1006 (1980).